Published in final edited form as:
Remote Sens Environ. 2019 October ; 232: . doi:10.1016/j.rse.2019.111344.

Diverse photosynthetic capacity of global ecosystems mapped by satellite chlorophyll fluorescence measurements

Liming He[a,b,*], **Jing M. Chen**[a,c], **Jane Liu**[a], **Ting Zheng**[d], **Rong Wang**[a], **Joanna Joiner**[e], **Shuren Chou**[f], **Bin Chen**[g], **Yang Liu**[g], **Ronggao Liu**[g], **Cheryl Rogers**[a]

[a]Department of Geography and Planning, University of Toronto, Toronto, ON M5S 3G3, Canada

[b]Laboratory of Environmental Model and Data Optima, Laurel, MD 20707, USA

[c]International Institute for Earth System Sciences, Nanjing University, 210023 Nanjing, China

[d]Department of Forest and Wildlife Ecology, University of Wisconsin, Madison, WI 53706, USA

[e]NASA Goddard Space Flight Center, Greenbelt, MD 20771, USA

[f]Space Engineering University, Beijing 101419, China

[g]China State Key Laboratory of Resources and Environmental Information System, Institute of Geographic Sciences and Natural Resources Research, Chinese Academy of Sciences, Beijing 100101, China

Abstract

Photosynthetic capacity is often quantified by the Rubisco-limited photosynthetic capacity (i.e. maximum carboxylation rate, V_{cmax}). It is a key plant functional trait that is widely used in Earth System Models for simulation of the global carbon and water cycles. Measuring V_{cmax} is time-consuming and laborious; therefore, the spatiotemporal distribution of V_{cmax} is still poorly understood due to limited measurements of V_{cmax}. In this study, we used a data assimilation approach to map the spatial variation of V_{cmax} for global terrestrial ecosystems from a 11-year-long satellite-observed solar-induced chlorophyll fluorescence (SIF) record. In this SIF-derived V_{cmax} map, the mean V_{cmax} value for each plant function type (PFT) is found to be comparable to a widely used N-derived V_{cmax} dataset by Kattge et al. (2009). The gradient of V_{cmax} along PFTs is clearly revealed even without land cover information as an input. Large seasonal and spatial variations of V_{cmax} are found within each PFT, especially for diverse crop rotation systems. The distribution of major crop belts, characterized with high V_{cmax} values, is highlighted in this V_{cmax} map. Legume plants are characterized with high V_{cmax} values. This V_{cmax} map also clearly illustrates the emerging soybean revolution in South America where V_{cmax} is the highest among the world. The gradient of V_{cmax} in Amazon is found to follow the transition of soil types with different soil N and P contents. This study suggests that satellite-observed SIF is powerful in deriving the important plant functional trait, i.e. V_{cmax}, for global climate change studies.

*Corresponding author at: Department of Geography and Planning, University of Toronto, Toronto, ON M5S 3G3, Canada. hel@geog.utoronto.ca (L. He).

Appendix A. Supplementary documents
Supplementary data to this article can be found online at https://doi.org/10.1016/j.rse.2019.111344.

Keywords

V_{cmax}; Photosynthetic capacity; Maximum carboxylation rate; Global; Climate change; Chlorophyll fluorescence; Ecosystem

1. Introduction

Plant functional traits are fundamental to ecological studies (Diaz et al., 2016; Kattge et al., 2011; Kunstler et al., 2016; Levine, 2016). The Rubisco-limited photosynthetic capacity (i.e. maximum carboxylation rate, V_{cmax}) is among these traits that have large interspecific and intraspecific variations. V_{cmax} also varies strongly with time and space within the same plant function type, depending on radiation and nutrient availabilities (Misson et al., 2006). Our understanding of the spatiotemporal distributions of V_{cmax} and its response to changing climate can help project carbon sequestration by vegetation and future climate change (Madani et al., 2018; A. P. Walker et al., 2017).

The availability of measured V_{cmax} data is limited because V_{cmax} is traditionally determined by measuring A-Ci curves, which is rather laborious (Kauwe et al., 2016; Xu and Baldocchi, 2003). Currently, Earth System Models (ESMs) heavily rely on meta-analysis based V_{cmax} databases which are derived from the correlation between leaf N content and V_{cmax} (Kattge et al., 2009). V_{cmax} also has strong seasonal variations (Jin et al., 2012; Wang, 2008; Wang et al., 2004; Wang et al., 2009a, 2009b). The value of V_{cmax} is often set as a constant for each plant function type (PFT) in terrestrial biosphere models, and the uncertainty in V_{cmax} has hampered our understanding of global carbon and water cycles (Bonan et al., 2012; Harper et al., 2016; L. M. He et al., 2017; Madani et al., 2018).

Recent advances in remote sensing make it possible to directly derive V_{cmax} for large areas from remotely sensed satellite observations. Recently, Alton (2018) mapped global V_{cmax} from satellite observations of chlorophyll content. However, the derived leaf V_{cmax} values are lower and vary more narrowly than compiled measurements. Carter et al. (1996) showed the promise of solar-induced chlorophyll fluorescence (SIF) in capturing photosynthetic capacity at the leaf level. Recent studies show that spaceborne SIF has a strong correlation with gross primary productivity (GPP) (Joiner et al., 2018; MacBean et al., 2018; Sun et al., 2018; Sun et al., 2017a) and thus it is promising to derive V_{cmax} from SIF (Koffi et al., 2015), e. g. for cropland (Y. Zhang et al. 2018; Zhang et al., 2014).

Photosynthesis involves two processes. The first one is light-dependent: light energy is harvested and converted into chemical energy in the form of electron carrying molecules like ATP and NADPH in Photosystems I and II (PS I and PS II) in the thylakoid membranes of chloroplasts. When a chlorophyll pigment absorbs visible light, it becomes excited and will return to the ground state by one of several competing processes, including photosynthesis in PS II, non-radiative decay, nonphotochemical quenching, and fluorescence. The yield fluorescence is generally small (1%–5%) but the signal is enough to provide information on the total amount of light absorbed, as the fluorescence is generally proportional to the total amount of absorbed photosynthetically active radiation (APAR) (Frankenberg and Berry, 2018). In the second process (i.e., the Calvin cycle), which is light-independent, carbohydrate molecules are assembled from CO_2 using the chemical energy harvested during the light-dependent reactions. In this process, Ribulose-1, 5-bisphosphate carboxylase/oxygenase (Rubisco) is the enzyme involved in the first major step of carbon fixation. Rubisco catalyzes the carboxylation of ribulose-1,5-bisphosphate (i.e. RuBP). However, Rubisco is able to fix only 3–10 CO_2 molecules each second per molecule of enzyme (Bar-On and Milo, 2019). The reaction catalyzed by Rubisco is, thus, the primary limiting factor of the Calvin cycle at sunlit conditions. Therefore, V_{cmax} (the maximum rate of carboxylation of Rubisco; μmol CO_2 m^{-2} s^{-1}) is largely determined by the amount of Rubisco in the leaf.

Although the Calvin cycle does not use light as a reactant, it requires the products of the light-dependent reactions (energy carrying molecules, e. g., ATP and NADPH) to drive the construction of new carbohydrate molecules. After the energy is transferred, the energy carrying molecules return to the light-dependent reactions to obtain more energized electrons. In addition, several enzymes of the light-independent reactions are activated by light (Bar-On and Milo, 2019). Therefore, these two processes are tightly coupled.

In a leaf, nitrogen plays an important role in regulating the photosynthetic capacity as it is a component of pigments for light harvest, proteins associated with photosystems and Calvin cycle (including Rubisco), ATP and NADP. Plants require an optimized balance of light intensity and carbon assimilation in the process of photosynthesis for survival when environmental conditions are ideal and for acclimation when environmental conditions are severe (Smith et al., 2019). For a leaf acclimated to the environment, the allocation of N to light harvesting pigments (chlorophylls) and carboxylation enzymes (Rubisco) would be optimized in a way that they become highly correlated. Studies have found that chlorophyll content correlates well with V_{cmax} which is largely determined by the amount of Rubisco (Croft et al., 2017; Luo et al., 2019). Therefore, chlorophyll can be a useful indicator for the carboxylation capacity of a leaf (Murchie and Lawson, 2013). As sun-induced chlorophyll fluorescence (SIF) is not only determined by chlorophyll content but also by radiation and other environmental variables, we cannot relate SIF to V_{cmax} directly. However, we can use a numerical technique to estimate and remove the effects of other factors in SIF signals and extract the needed V_{cmax}. The data assimilation technique presented in this paper is developed for this purpose.

Excessive light may damage the photosynthetic machinery. The correlation between SIF and photosynthesis assimilation rate will certainly not be held for a leaf without water supply under sunlight, as photosynthesis needs water (to provide electrons from hydrogen atoms, and for heat dissipation). At such an extremely stressed condition, the absorbed light energy excites the pigment but the native energy or the electron acceptor is missing. The energy can then be used to excite oxygen and produce singlet oxygen molecules, which decompose chlorophylls. In this case, SIF may not be an indicator of the photosynthesis rate.

However, a plant reacts to mitigate the harmful effects of excess light in natural settings (i.e., via photoprotection). For example, some plants can change the leaf inclination angle to reduce the incident light on the leaf surface. Under persistent droughts over days and weeks, plants can develop mechanisms (photo-acclimatization) of up-regulation of stress response proteins or down-regulation of pigment biosynthesis. For example, PS II is damaged by light irrespective of light intensity, and has a repair cycle as the chloroplast acclimation strategy to irradiance stress. The PS II repair cycle occurs in chloroplasts and in cyanobacteria, consisting of degradation and synthesis of the D1 protein of the PSII reaction center, followed by activation of the reaction center. However, environmental stresses, for example, extreme temperatures, salinity, and drought (Zhu et al., 2017), limit the supply of CO_2 for use in carbon fixation, which in turn decreases the rate of repair of PSII. In autumn, many plants stop making chlorophylls and break down chlorophylls into smaller molecules in responding to cold. The decreases of light-harvesting and activity of the Calvin cycle tend to be synchronized; therefore, SIF has been used to track photosynthesis even under drought conditions (Gonsamo et al., 2019; Jiao et al., 2019; Y. Sun et al., 2015).

A spaceborne instrument is only able to observe a fraction of SIF escaped from the canopy, and these fractions vary greatly with the sun-target-satellite observation geometry and complex canopy structure (He et al., 2017b; Z. Zhang et al. 2018). Therefore, although the SIF-GPP correlation is strong, it is also found that the SIF-to-GPP ratio varies with PFT and location (Li et al., 2018a; Wood et al., 2017; Zhang et al., 2016a, 2016b), hindering the derivation of global V_{cmax} maps using SIF. Norton et al. (2018) averaged the OCO-2 SIF data into 2° × 2° grids, assimilated these SIF data into a combined ecosystem model (BETHY-SCOPE) with prescribed leaf area index (LAI) as input and found that the simulation of global GPP is improved; however, SCOPE (van der Tol et al., 2009) utilizes the SAIL5 model (Verhoef, 1984) which is a 1D radiative transfer model, therefore, they did not make full use of vegetation structure information (such as clumping) in their framework, neither was global V_{cmax} map produced from their study.

The objective of this study is to map the spatiotemporal distribution of V_{cmax} for global terrestrial ecosystems by reconciling the variations in the SIF-to-GPP ratio in ecosystems due to changes in observation geometry and canopy structure. In the following, we present the major findings for the top-of-canopy V_{cmax} that is normalized to 25 °C ($V_{cmax,}$ 25^0) unless specified otherwise.

2. Materials and methods

2.1. Forcing data, SIF data, and key model parameters

A complete description of meteorological forcing data (Rienecker et al., 2011), GOME-2 SIF data (Joiner et al., 2013) and the BEPS model (Boreal Ecosystem Productivity Simulator) (He et al., 2018) for Gross Primary Production (GPP) simulation and its key model parameters is provided in the Supplementary materials. A Leaf Area Index (LAI) product (named GLOBMAP) (Liu et al., 2012) is used to drive BEPS. A clumping index map is used to describe the canopy structure (L. He et al., 2012; He et al., 2016).

Ground measurements of SIF from winter wheat were also made using an automated multi-angle chlorophyll fluorescence measurement system (SI). The measurements took place at a flux tower site (Jurong station, 31°9′N, 119°1′E) in Jiangsu province, China. The SIF was observed during 15th April to 30th May in 2016 when the wheat canopy was closed. The

SIF measurements, together with LAI, GPP from this site are used to derive the SIF-GPP relationship.

2.2. The "two-leaf" ecosystem model for simulation of vegetation productivity

A detailed description of BEPS is provided in the supplementary materials. In this section, we summarize the key BEPS modules that are related to V_{cmax} and GPP modeling. BEPS is spun up from 1981 to 2006 using the forcing data. In this study, we modified the BEPS to output GPP from sunlit leave for SIF retrieval. At the leaf level, Farquhar's model is used to calculate the net CO_2 assimilation rate (Farquhar et al., 1980). In Farquhar's model, the CO_2 assimilation rate is either determined by Rubisco-limited or light-limited gross photosynthetic rates (see details in Supplementary material, Section 2.2). At light-saturated condition (for sunlit leaves), V_{cmax} and leaf temperature are two of the most important parameters that control Rubisco-limited gross photosynthetic rates (μmol m^{-2} s^{-1}); while at light-limited condition, J_{max}, radiation and leaf temperature are three of the most important parameters for the calculation of the gross photosynthetic rate. Although Farquhar's model is included in many ESMs as the core photosynthesis module for almost four decades, these ESMs still rely on tabulated V_{cmax} values for each ecosystem with no consideration of their spatial variations. BEPS uses a "two-leaf" approach to calculate the canopy level CO_2 assimilation (Chen et al., 1999; Norman, 1982). The key parameter V_{cmax} is also upscaled weighted by the leaf nitrogen profile in the canopy (Chen et al., 2012). The objective of this paper is to globally map $V_{cmax,0}$, the maximum Rubisco capacity at the leaf level at the top of the canopy that is normalized at 25 °C.

2.3. The normalization of satellite SIF observation to the hotspot direction

Exposed at different radiation conditions, sunlit and shaded leaves differ in their SIFs, which can vary as large as an order of magnitude (Pinto et al., 2016). Additionally, there are large variations of SIF signals observed from different solar and satellite view geometries (Liu et al., 2016; Z. Zhang et al., 2018). The escape probability of SIF is also affected by canopy structure. For example, leaves in cropland are distributed most randomly among all vegetation types; therefore, the sunlit leaves of crops are mostly distributed at the top of the canopy and can be largely observed at different satellite view angles; however, the sunlit leaves of forests can be located in the low parts of a canopy due to their complex 3-dimensional structure and thus the portion of observed sunlit leaves, where the most SIF signal originates, depends on view angles. Therefore, the global maximum SIF signal is often observed from croplands but not from forests, although forests are the most productive ecosystems.

To reliably estimate the ratio of observed SIF (especially the SIF from sunlit leaves) to the total emitted SIF, we need a well-documented geometric optical model, such as the 4-Scale model (Chen and Leblanc, 1997) and vegetation structure parameters, including LAI (Liu et al., 2012) and clumping index (L. M. He et al., 2012). Especially, the global clumping index provides unique information regarding to the leaf distributions in different ecosystems, which frees us from the requirement of homogenous canopy in order to calculate the ratio of observed sunlit leaves, which is key to SIF escape probability. For global applications, we have simplified the 4-Scale model to estimate the escape probability of SIF from canopy at different angles (He et al., 2017b). The methodology is detailed in the SI.

Here, we applied the previously developed method to normalize GOME-2 clear-sky SIF measurements to the hotspot direction (Chen and Leblanc, 1997; He et al., 2017b); in other words, the normalization gives an estimate of the maximum SIF signal that can be observed in a canopy from a satellite from the hotspot direction.

2.4. The relationship between "hotspot SIF" and GPP from sunlit leaves

Previously, the canopy level SIF-to-GPP ratio has been directly used to constrain global GPP simulations (Joiner et al., 2018; MacBean et al., 2018). As aforementioned, the SIF-to-GPP ratio at the canopy level can be affected by both satellite view angle and vegetation structure; therefore, previous studies often relied on time-averaged SIF-to-GPP ratios calibrated for different ecosystems.

In this study, we propose to use "hotspot SIF" to constrain "sunlit GPP" simulation in an ecosystem model, such as BEPS. In theory, this "hotspot SIF" to "sunlit GPP" ratio is independent of both view angle and vegetation structure if assuming a uniform leaf inclination angle, and thus ecosystem-based calibration of the ratio is no longer necessary. We can explicitly use a BRDF model and vegetation structural parameters (i. e. LAI and clumping index) to minimize uncertainties in the SIF-to-GPP ratio at the canopy level among ecosystems.

Moreover, we choose to constrain "sunlit GPP" not the total GPP in our simulations because the photosynthesis at the hotspot direction is light-saturated (see Eq. (2)) under clear-sky condition when GOME-2 SIF is collected. Therefore, the modeling of sunlit GPP in BEPS is less prone to uncertainties induced by the radiation input data.

Another reason to constrain "sunlit GPP" not the total GPP is that the calculation of sunlit LAI in BEPS is less prone to the uncertainties of the total LAI (see Eqs. (6) and (7)). As shown in the SI, sunlit LAI does not increase proportionally to the increase of total LAI; the magnitude of sunlit LAI is largely stable when total LAI is larger than 2.

The "hotspot SIF" to "sunlit GPP" ratio is determined in two ways (see more details in SI). In the first approach, we (1) simulate sunlit-GPP in BEPS using the default V_{cmax} map which is derived according to land cover type and tabulated V_{cmax} from Kattge et al. (2009), (2) derive the "hotspot SIF" (corrected from GOME-2) to "sunlit GPP" ratio for each pixel, (3) create a histogram of this "hotspot SIF" to "sunlit GPP" ratio from the global simulation, and (4) choose the mode of this histogram (Fig. S4(a) and (b), SI). In the second approach, we estimate this ratio directly from measured SIF and measured GPP at a flux tower site (Fig. S4(c)). In the end, both approaches reach a similar ratio, 4.1 mW m^{-2} nm^{-1} sr^{-1}/(g C m^{-2} h^{-1}) and then this unique ratio is applied to all ecosystems without further calibration. We suggest that the value of this ratio should be further calibrated according to the features of a specific sensor (band width, spectral resolution for SIF retrieval) if it is applied to another SIF product.

2.5. The data assimilation framework for V_{cmax} retrieval

In this study, we do not directly invert V_{cmax} from SIF; instead, we use an EnKF filter for parameter estimation (He et al., 2014; Mo et al., 2008; Schöniger et al., 2012). EnKF for parameter optimization is optimal for ill-posed inversion problems (Iglesias et al., 2013) because the parameter (V_{cmax} in this study) is updated in a system that synthesizes prior knowledge and new observations by statistical minimization of estimation errors. This is ideal for V_{cmax} retrieval as V_{cmax} evolves smoothly along the leaf nitrogen changes.

The normalization of GOME-2 SIF to the hotspot direction tightly follows the same strategy to separate sunlit and shaded leaves in BEPS. This enables us to directly constrain sunlit GPP in BEPS using hotspot SIF. We optimize the ecosystem model parameter, top-of-canopy maximum carboxylation rate ($V_{cmax,0}$, normalized to 25 °C), in a parallel data assimilation system run on a high performance computer (He et al. 2017a; He et al., 2014). This system has been used to assimilate soil moisture data from the SMAP mission into BEPS; for this study, it follows the same theory to adjust the BEPS model status (i.e., V_{cmax}) by assimilating GPP "observations" from GOME-2. The description of EnKF is summarized in SI.

We start to run 80 BEPS model replicates in the system since 2007 with perturbed V_{cmax} having an average value equal to the original BEPS V_{cmax} input (and one standard deviation of 12 μmol m^{-2} s^{-1}) (Fig. 1). Considering that there might be inconsistency of cloud conditions between forcing data and GOME-2 product, we only perform the parameter optimization when both forcing data and GOME-2 observations indicate clear-sky conditions. For each grid, whenever a GOME-2 SIF observation is available, it is normalized to hotspot direction and converted into sunlit GPP to constrain BEPS-simulated "sunlit GPP" for V_{cmax} retrieval. Currently, there is no much information available regarding the uncertainty of the GOME-2 SIF signal. When SIF is quality controlled and gridded to half degree spatial resolution and biweekly time frame, the estimated absolute error is 0.1–0.4 mW m^2 nm^{-1} sr^{-1} (Joiner et al., 2013; Joiner et al., 2016). Since the instantaneous SIF observations are used, we choose 0.5 mW m^2 nm^{-1} sr^{-1} in this study. This generally means that higher SIF signal has less relative uncertainty and has stronger constraints in the system for V_{cmax} retrieval. The optimized V_{cmax} is then used in the next step for the simulation of both sunlit and shaded GPP in BEPS until the next V_{cmax} retrieval is available. An 11-year-long record of V_{cmax} (2007–2017) is produced in this study based on GOME-2 SIF observations.

3. Results

3.1. Spatial distribution of V_{cmax}

The retrieved V_{cmax} has strong seasonal and inter-annual variations. The 11-year mean and standard deviation of V_{cmax} are shown in Fig. 2 and Table 1.

The distinct belts of boreal forests in the northern hemisphere have the lowest V_{cmax} values and variations (44.6 ± 2.7 μmol m^{-2} s^{-1} for deciduous needleleaf forests, DNF, and 48.2 ± 5.7 μmol m^{-2} s^{-1} for evergreen needleleaf forests, ENF, respectively). These values and their ranges are similar to previous findings at flux tower sites (He et al., 2014; Zheng et al., 2017). Note that there are different definitions in LAI and V_{cmax} in term of “leaf area” for non-flat leaves. We used a definition by Chen and Black (1992b) which defines LAI as the half the total intercepting area per unit ground surface area; while the V_{cmax} values reported in the previous literature might use “per projected leaf area”. Considering the difference in “leaf area”, the V_{cmax} values derived under two LAI definitions will differ by a factor of ~$\pi/2$ (projecting cylinder to plate).

Evergreen broadleaf forests (EBF) also have relatively low V_{cmax} (53.6 ± 14.7 μmol m^{-2} s^{-1}) around the equator but with large spatial variations. In the retrieved V_{cmax} map, we find that the V_{cmax} gradient in Amazon follows the transition of Oxisol soil (lack of P) to Ultisol soil (non-Oxisol) (Fig. 2c). This is consistent with the study by Kattge et al. (2009) who found that V_{cmax} is strongly correlated to leaf nitrogen (N) content and reported V_{cmax} values in tropical trees for oxisols soil and non-oxisols soil, respectively, and the sensitivity of V_{cmax} to leaf N is increased with increasing leaf phosphorus (P) (Walker et al., 2014). This result also echoes the mechanistic model by Ali et al. (2016) that shows a clear gradient of V_{cmax} in Amazon (their Fig. 4, and SI).

The V_{cmax} values in shrublands have the largest spatial variation (57.4 ± 31.0 μmol m^{-2} s^{-1}); the V_{cmax} values from this study are close to the median V_{cmax} (60 μmol m^{-2} s^{-1}) of Shrub in the Caatinga biome, eastern Brazil, from two field campaigns (Rezende et al., 2016). Deciduous broadleaf forests (DBF), often mixed with croplands, have a moderately high V_{cmax} and spatial variation among all PFTs (72.7 ± 14.7 μmol m^{-2} s^{-1}). The V_{cmax} values for grassland are the highest (88.7 ± 20.9 μmol m^{-2} s^{-1}). With the inclusion of corn, which is a low V_{cmax} C4 crop, croplands have the second highest V_{cmax} (82.7 ± 15.2 μmol m^{-2} s^{-1}). V_{cmax} in croplands also has the strongest seasonal variation (Fig. 3b) due to agricultural management, e. g. cropping rotations. This V_{cmax} map clearly shows the global distribution of crop belts, e. g. the corn-soybean and wheat belts in US, wheat-corn belt in China, the super-high productive wheat-rice cropping system in Punjab, India (Kang et al., 2009; Khajuria, 2016; Singh et al., 2009), and two cropland belts in Australia (Supplementary figures).

Interestingly, we reveal a very high V_{cmax} belt in South America, which is associated with the rapid development of soybean cultivation in recent years (Correia, 2017; Fehlenberg et al., 2017; Gasparri et al., 2016; McKay et al., 2016; Mier y Terán Giménez Cacho, 2016), the so-called soybean revolution in South America (Cattelan and Dall’Agnol, 2018; Richards, 2010; Torres et al., 2017). During the last 35 years, the soybean production in South America is ten-fold increased (SI). According to http://www.fao.org/faostat/en/#data/QC/visualize, currently more than 80% of soybean are produced in America, while recently Brazil surpassed USA as the top soybean producer. The functional group of legume is well known for its high V_{cmax} (Ainsworth and Rogers, 2007; Feng and Dietze, 2013). As shown in Fig. 3(i), the retrieved V_{cmax} for croplands is as high as 220 μmol m^{-2} s^{-1}, comparable to the ranges of soybean V_{cmax} measurements (101–190 μmol m^{-2} s^{-1}) (Bunce, 2016; Morgan et al., 2004; B. J. Walker et al., 2017; Xu et al., 2016). We found that the soybean production (Cattelan and Dall’Agnol, 2018) in each Brazilian state can explain 52% of variance in V_{cmax} (SI).

The dervied V_{cmax} around coastal tundra in high Arctic is higher than orginal BEPS V_{cmax} input by 10–20 μmol m^{-2} s^{-1}. This higher V_{cmax} retrieval echos to recent measurements by Rogers et al. (2017). They attribed the high V_{cmax} in high Arctic area to two factors: (1) the higher leaf N content; and (2) more N is allocated in Rubisco. They also found that the V_{cmax} (normalized at 25 °C) was significantly higher than the inputs in current Earth System models by two- to five-folds.

Five distinctive features are found from our V_{cmax} map, including (1) gradients across major PFTs, (2) gradients within the Amazon forest from north to south, (3) global major crop belts, (4) high V_{cmax} in crop belt of South America, and (5) moderate to high V_{cmax} in northern tundra. Potential drivers (temperature, precipitation, radiation, LAI, root-zone dryness) of these V_{cmax} features are also examined (Figs. S25–S29). The transition of temperature itself from the tropic to the polar region cannot explain the V_{cmax} distribution. At low to middle latitudes, lower solar radiation is associated with higher cloud coverages (and more precipitation); the V_{cmax} gradient (low to high) from this study follows the transition of LAI (high values in forest in wet area to low values in grassland in dry area). However, water stress cannot explain the high V_{cmax} values in tundra areas. Temperature, precipitation and radiation cannot explain the V_{cmax} gradient within Amazon forests. The crop belts with high V_{cmax} values, which are dominated by anthropogenic activities, are not associated with extra high or lower LAI values (Fig. S25). Comparing the V_{cmax} patterns in crop belts of South America to maps in Figs. S19 to S29, we suggest that the soybean belt best explains these high V_{cmax} values.

3.2. Seasonal variation of V_{cmax}

The seasonal variations of V_{cmax} for nine locations are provided in Fig. 3. Due to clouds, the EBF has the least number of retrievals (Fig. 3(a)). EBF and ENF (Fig. 3(c)) have the least seasonal variations. V_{cmax} for ENF in the spring is overestimated due to the underestimation of LAI in this season (Wang et al., 2016). DBF (Fig. 3(b)) in US shows strong seasonal variation, increasing in the spring, peaking at early summer (day of year (DOY) = 180), and decreasing gradually in the fall.

Due to management practices, the seasonal variations of V_{cmax} for croplands show diversified patterns (Figs. 3(d)–3(i)). The US corn belt, a single cropping system (Fig. 3(d)), is characterized with a V_{cmax} maximum in August. The croplands in the southern hemisphere (Fig. 3(e, i)) have peaked V_{cmax} during the spring. Fig. 3(f) and (g) show that the high V_{cmax} of winter wheat in the spring is replaced by another crop in the summer with low V_{cmax} values (e. g. C4 corn) in Shandong, China. With adequate irrigation and fertilization, V_{cmax} in Punjabi croplands is among the highest in the world (Fig. 3h).

Only limited validation can currently be performed for this V_{cmax} map that is at 36 km resolution, because it is difficult to find pure pixels at this resolution and V_{cmax} has seasonal and inter-annual variations (Xu and Baldocchi, 2003). V_{cmax} also varies with the vertical N profile in the canopy (Domingues et al., 2005) and with environmental conditions (e. g. soil nutrition, water stress, and shading) (Dechant et al., 2017; Sharwood et al., 2014). Both types of information are limited in the literature. Ground observations suggest that the maximum V_{cmax} ranges from 105 to 150 μmol m^{-2} s^{-1} (Feng et al., 2011; Hu et al., 2014;

Silva-Pérez et al., 2017; J.S. Sun et al. 2015) for wheat and from 30.1 ± 3.5 to 40 ± 1 μmol m^{-2} s^{-1} (Massad et al., 2007; Sharwood et al., 2014) for maize (corn). It can be as high as 140 μmol m^{-2} s^{-1} (Borjigidai et al., 2006; Ikawa et al., 2018) for rice. The V_{cmax} values retrieved in this study are generally close to the upper range of ground values because retrieved values represent the top-of-canopy values which are higher than the average values for the canopy.

3.3. Impacts on global GPP simulation

Similar to other ecosystem models, the V_{cmax} values in the default BEPS are set according to vegetation types. After using the spatially and temporally explicit V_{cmax} maps in BEPS (Fig. 4(a–e)), the GPP estimation is reduced by 13% and 6% for ENF and croplands, respectively, due to decreased V_{cmax} (Table 2). In contrast, the GPP estimation is increased by 2%, 5%, 7%, 10%, and 1% for EBF, DNF, DBF, Shrub, and grassland, respectively. The GPP estimation for EBF at non-oxisol soil is significantly increased due to increased V_{cmax}. DBF in the US is highlighted with increased V_{cmax} and GPP. Although there is a remarkable increase of GPP in the croplands of South America, the global average GPP of croplands is decreased by 6% due to the stronger seasonal variation in derived V_{cmax} and crop rotations (e. g. with low V_{cmax} of corn).

Driving the model with the same LAI and meteorological data, the global GPP simulation with SIF-derived V_{cmax} is 126.3 ± 1.5 Pg C yr^{-1} (here the one standard deviation was derived from global GPP in 2007–2017; it is not an indicator of uncertainty). This contrasts to the GPP simulation using the seasonal invariable V_{cmax} (130.4 ± 2.2 Pg C yr^{-1}) which could lead to overestimate of GPP in the spring and autumn.

4. Discussion

4.1. Why do we choose “hotspot SIF” to constrain “sunlit GPP”?

Like other remote sensing products, the accuracy of this new V_{cmax} map depends on the accuracies of the ecosystem model used for V_{cmax} optimization and the input data, such as LAI, clumping index, SIF data, metrological data and the SIF-to-GPP ratio.

As aforementioned, we have chosen to use “hotspot SIF” to constrain “sunlit GPP” rather than to use “total SIF” to constrain “total GPP”. This approach is necessary for the conversion from the canopy-level SIF measurements to the leaf-level information retrieval. It also has the advantage that that both the modeling of “hotspot SIF” and “sunlit GPP” are less prone to uncertainties in input parameters.

The modeling of sunlit GPP depends on the simulations of (1) sunlit LAI and (2) Rubisco-limited gross photosynthetic rates. In Section 2.4, we have shown that the magnitude of sunlit LAI is not sensitive to the multiplication of “total LAI and clumping index” when LAI is relatively large. This is because the uncertainty in total LAI mostly goes to the shaded part in the BEPS two-leaf scheme. Comparing to light-limited GPP modeling at the leaf level which requires three major parameters (J_{max}, leaf temperature and radiation) as inputs, the Rubisco-limited GPP modeling does not require radiation as input which has much uncertainty. By using hotspot SIF, our framework is not very sensitive to the uncertainty in the meteorological forcing data (except temperature, which usually has less uncertainty).

4.2. Towards to a unique GPP-SIF ratio

Using "hotspot SIF" frees us from using ecosystem-based calibrations. Determining a unique SIF-to-GPP ratio across biomes is at the cutting edge of SIF studies (Duveiller and Cescatti, 2016; Frankenberg et al., 2011; Guan et al., 2016; Joiner et al., 2014; Li et al., 2018b; Liu et al., 2017; Luus et al., 2017; Verma et al., 2017; Verrelst et al., 2016; Wagle et al., 2016; Walther et al., 2016; Wang, 2014; Wood et al., 2017; Yang et al., 2016; Yang et al., 2015; Yoshida et al., 2015; Zhang et al., 2016a, 2016b), while previous studies were hindered by ignoring the variation of the SIF signal due to the variation of the shadow fraction with view angle. For example, it was found that there are small variations in the "total GPP"-to-"average SIF" slopes (4.60–5.55 g C m^{-2} day^{-1}/(mWm^{-2} nm^{-1} sr^{-1})) (Zhang et al., 2016a, 2016b), which are equivalent to "average SIF"-to-"total GPP" ratio of 4.3 to 5.2 mW m^{-2} nm^{-1} sr^{-1}/(g C m^{-2} h^{-1}). The variation of this slope should be reduced once the SIF signal is normalized to the hotspot direction, from which shadows are invisible. Combining a unique clumping index derived from multiple-angular MODIS data and a sophisticated geometric optical model advances the way to derive the "hotspot SIF"-to-"sunlit GPP" ratio in this study (Chen and Leblanc, 1997; He et al., 2017b). Field observations at flux tower sites, although limited, also yield the same SIF-to-GPP ratio (4.1 mW m^{-2} nm^{-1} sr^{-1}/ (g C m^{-2} h^{-1})), further supporting the "meta-based" analysis from the global GPP simulation in this study.

Besides the strong arguments on the similarity of the GPP-SIF slope across PFTs (Li et al., 2018b; Xiao et al., 2019; Z. Zhang et al., 2018), Liu et al. (2017) found that the slope is higher for C4 crops than for C3 plants. This is because the C4 plants have less photorespiration and are more efficient in photosynthesis, and therefore C4 plants emit less SIF for the same amount of photosynthesis than C3 plants. Currently, the information on the GPP-SIF slope for C4 plants is still limited. In this study, we used a C3 model and potentially this suggests that the GPP may be underestimated for regions where C4 plants dominate; however, given our current framework, a separate GPP-SIF slope can be taken whenever the slope information becomes more certain and the location and period of C4 plantation become clearer in future.

4.3. Comparison of result to previous dataset

The SIF-derived V_{cmax} from this study is compared to a widely used N-derived V_{cmax} dataset (Fig. 5) (Kattge et al., 2009). Although both datasets show comparable magnitudes (R^2 = 0.61) and variations, they diverge in the magnitudes of V_{cmax} for ENF, with higher values in N-derived V_{cmax}. This may be explained by the use of different LAI definitions for non-flat leaves: we use true LAI, defined as the half total intercepting area, while Kattge et al. (2009) may use projected LAI with lower values (Chen and Black, 1992a).

4.4. Future studies

We realize that V_{cmax} measurements from flux towers at a footprint of ~500 m may not match our retrievals at 36 km resolution. Two future efforts will be highly useful in validating our proposed framework of V_{cmax} mapping: (1) making use of available SIF measurements at high spatial resolutions. These measurements include OCO-2 and OCO-3 data at the spatial resolution of 1.1 km (Sun et al., 2017b) and TRO-POMI data at the spatial resolution of 3.5 × 7 km^2 (Köhler et al., 2018). Especially OCO-3 has the capability to point to a specific flux tower site for multi-times in a day. This gives the opportunity to compare V_{cmax} retrievals from satellite imagery to eddy-covariance based retrievals (Zheng et al., 2017). (2) making ground measurement of SIF using ultra-high resolution hyperspectral sensors (Xi Yang et al., 2018). Hotspot SIF measurements from these ground systems can be used to invert V_{cmax} values that can be compared to direct V_{cmax} measurements from A/Ci curves (Manter and Kerrigan, 2004).

5. Conclusions

Based on the strong correlation between SIF and GPP, this study uses a data assimilation approach to derive a long-term product (2007–2017) of top-of-canopy V_{cmax} at the leaf level (normalized to 25 °C) from GOME2 SIF data. A critical step in this approach is to use angularly-normalized instantaneous SIF in the hotspot direction to constrain simulated GPP from sunlit leaves in order to account for different probabilities of observing sunlit leaves from different view directions relative to the sun. In conclusion, we have the following major findings:

1. The range of the SIF-derived V_{cmax} retrievals are comparable to documented V_{cmax} values in the literature. The V_{cmax} map shows distinct belts associated with the distribution of plant function types (PFT). Within each PFT, V_{cmax} also varies greatly, except for conifers. In the Amazon evergreen broadleaf forests, the retrieved V_{cmax} is sensitive to soil type and hence possibly P limitation, with a V_{cmax} gradient along the transition of soil orders.

2. Seasonal variation of V_{cmax} depends largely on PFTs and locations. Agricultural activities, such as crop rotation and fertilizer use, can strongly impact both temporal and spatial variations of V_{cmax} in croplands. All well-known crop belts in different continents are clearly illustrated on the derived V_{cmax} map. Characterized with high V_{cmax}, the booming soybean revolution in South America is also clearly shown on the map.

A great deal of effort is needed to validate this V_{cmax} map. Due to the large spatio-temporal variations of V_{cmax}, low-cost and standardized V_{cmax} measurements for the large pixels are yet to be developed.

Supplementary Material

Refer to Web version on PubMed Central for supplementary material.

Acknowledgement

J. M. Chen was partially supported by the National Key Research and Development Program of China (2016YFA0600202). J. M. Chen and L. He was supported by Canadian Space Agency grant (14SUSMAPTO). R. Wang was supported by Canadian Space Agency grant (17SUSOARTO). T. Zheng was supported by the Townsend Lab at the University of Wisconsin-Madison through funding support provided by Jet Propulsion Laboratory contract 1579654. R. Liu was supported by International Cooperation and Exchange Programs of National Science Foundation of China (Sino-German, 41761134082). The data processing is impossible without the SciNet high performance computer resource and the support from SciNet Staff. The V_{cmax} map derived from this study will be published at the first author's ResearchGate: https://www.researchgate.net/profile/Liming_He4.

References

Ainsworth EA, Rogers A, 2007 The response of photosynthesis and stomatal conductance to rising [CO2]: mechanisms and environmental interactions. Plant Cell Environ. 30 (3), 258–270. 10.1111/j.1365-3040.2007.01641.x. [PubMed: 17263773]

Ali AA, Xu C, Rogers A, Fisher RA, Wullschleger SD, Massoud EC, … Wilson CJ, 2016 A global scale mechanistic model of photosynthetic capacity (LUNA V1.0). Geosci. Model Dev 9 (2), 587–606. 10.5194/gmd-9-587-2016.

Alton PB, 2018 Decadal trends in photosynthetic capacity and leaf area index inferred from satellite remote sensing for global vegetation types. Agric. For. Meteorol 250, 361–375.

Bar-On YM, Milo R, 2019 The global mass and average rate of rubisco. Proc. Natl. Acad. Sci 116 (10), 4738–4743. 10.1073/pnas.1816654116. [PubMed: 30782794]

Bonan GB, Oleson KW, Fisher RA, Lasslop G, Reichstein M, 2012 Reconciling leaf physiological traits and canopy flux data: use of the TRY and FLUXNET databases in the Community Land Model version 4. Journal of Geophysical Research-Biogeosciences 117.

Borjigidai A, Hikosaka K, Hirose T, Hasegawa T, Okada M, Kobayashi K, 2006 Seasonal changes in temperature dependence of photosynthetic rate in rice under a free-air CO2 enrichment. Ann. Bot 97 (4), 549–557. [PubMed: 16399793]

Bunce J, 2016 Variation among soybean cultivars in mesophyll conductance and leaf water use efficiency. Plants 5 (4), 44 10.3390/plants5040044.

Carter GA, Jones JH, Mitchell RJ, Brewer CH, 1996 Detection of solar-excited chlorophyll a fluorescence and leaf photosynthetic capacity using a Fraunhofer line radiometer. Remote Sens. Environ 55 (1), 89–92. 10.1016/0034-4257(95)00192-1.

Cattelan AJ, Dall'Agnol A, 2018 The rapid soybean growth in Brazil. OCL 25 (1), D102.

Chen JM, Black TA, 1992a Defining leaf-area index for non-flat leaves. Plant Cell and Environment 15 (4), 421–429.

CHEN JM, BLACK TA, 1992b Defining leaf area index for non-flat leaves. Plant Cell Environ. 15 (4), 421–429. 10.1111/j.1365-3040.1992.tb00992.x.

Chen JM, Leblanc SG, 1997 A four-scale bidirectional reflectance model based on canopy architecture. IEEE Trans. Geosci. Remote Sens 35 (5), 1316–1337.

Chen JM, Liu J, Cihlar J, Goulden ML, 1999 Daily canopy photosynthesis model through temporal and spatial scaling for remote sensing applications. Ecol. Model 124 (2–3), 99–119. 10.1016/S0304-3800(99)00156-8.

Chen JM, Mo G, Pisek J, Liu J, Deng F, Ishizawa M, Chan D, 2012 Effects of foliage clumping on the estimation of global terrestrial gross primary productivity. Glob. Biogeochem. Cycles 26 doi:Artn Gb1019Doi 10.1029/2010gb003996.

Correia JE, 2017 Soy states: resource politics, violent environments and soybean territorialization in Paraguay. J. Peasant Stud 1–21. 10.1080/03066150.2017.1384726.

Croft H, Chen JM, Luo X, Bartlett P, Chen B, Staebler RM, 2017 Leaf chlorophyll content as a proxy for leaf photosynthetic capacity. Glob. Chang. Biol 23 (9), 3513–3524. 10.1111/gcb.13599. [PubMed: 27976452]

Dechant B, Cuntz M, Vohland M, Schulz E, Doktor D, 2017 Estimation of photosynthesis traits from leaf reflectance spectra: correlation to nitrogen content as the dominant mechanism. Remote Sens. Environ 196, 279–292.

Diaz S, Kattge J, Cornelissen JHC, Wright IJ, Lavorel S, Dray S, … Gorne LD, 2016 The global spectrum of plant form and function. Nature 529 (7585), 167–U173. [PubMed: 26700811]

Domingues TF, Berry JA, Martinelli LA, Ometto JPHB, Ehleringer JR, 2005 Parameterization of canopy structure and leaf-level gas exchange for an eastern Amazonian tropical rain forest (Tapajós National Forest, Pará, Brazil). Earth Interact. 9 (17), 1–23. 10.1175/ei149.1.

Duveiller G, Cescatti A, 2016 Spatially downscaling sun-induced chlorophyll fluorescence leads to an improved temporal correlation with gross primary productivity. Remote Sens. Environ 182, 72–89.

Farquhar GD, Caemmerer SV, Berry JA, 1980 A biochemical-model of photosynthetic Co2 assimilation in leaves of C-3 species. Planta 149 (1), 78–90. 10.1007/Bf00386231. [PubMed: 24306196]

Fehlenberg V, Baumann M, Gasparri NI, Piquer-Rodriguez M, Gavier-Pizarro G, Kuemmerle T, 2017 The role of soybean production as an underlying driver of deforestation in the South American Chaco. Glob. Environ. Chang 45, 24–34. 10.1016/j.gloenvcha.2017.05.001.

Feng X, Dietze M, 2013 Scale dependence in the effects of leaf ecophysiological traits on photosynthesis: Bayesian parameterization of photosynthesis models. New Phytol. 200 (4), 1132–1144. 10.1111/nph.12454. [PubMed: 23952643]

Feng ZZ, Pang J, Kobayashi K, Zhu JG, Ort DR, 2011 Differential responses in two varieties of winter wheat to elevated ozone concentration under fully open-air field conditions. Glob. Chang. Biol 17 (1), 580–591.

Frankenberg C, Berry J, 2018 3.10 - solar induced chlorophyll fluorescence: origins, relation to photosynthesis and retrieval In: Liang S. (Ed.), Comprehensive Remote Sensing. Elsevier, Oxford, pp. 143–162.

Frankenberg C, Fisher JB, Worden J, Badgley G, Saatchi SS, Lee JE, … Yokota T, 2011 New global observations of the terrestrial carbon cycle from GOSAT: patterns of plant fluorescence with gross primary productivity. Geophys. Res. Lett 38.

Gasparri NI, Kuemmerle T, Meyfroidt P, le de Waroux Polain Y, Kreft H, 2016 The emerging soybean production frontier in Southern Africa: conservation challenges and the role of south-south telecouplings. Conserv. Lett 9 (1), 21–31. 10.1111/conl.12173.

Gonsamo A, Chen JM, He L, Sun Y, Rogers C, Liu J, 2019 Exploring SMAP and OCO-2 observations to monitor soil moisture control on photosynthetic activity of global drylands and croplands. Remote Sens. Environ. 232, 111314. 10.1016/j.rse.2019.111314.

Guan KY, Berry JA, Zhang YG, Joiner J, Guanter L, Badgley G, Lobell DB, 2016 Improving the monitoring of crop productivity using spaceborne solar-induced fluorescence. Glob. Chang. Biol 22 (2), 716–726. 10.1111/gcb.13136. [PubMed: 26490834]

Harper AB, Cox PM, Friedlingstein P, Wiltshire AJ, Jones CD, Sitch S, … van Bodegom P, 2016 Improved representation of plant functional types and physiology in the Joint UK Land Environment Simulator (JULES v4.2) using plant trait information. Geosci. Model Dev 9 (7), 2415–2440.

He L, Chen JM, Pisek J, Schaaf CB, Strahler AH, 2012a Global clumping index map derived from the MODIS BRDF product. Remote Sens. Environ 119 (0), 118–130. 10.1016/j.rse.2011.12.008.

He LM, Chen JM, Pisek J, Schaaf CB, Strahler AH, 2012b Global clumping index map derived from the MODIS BRDF product. Remote Sens. Environ 119, 118–130. 10.1016/j.rse.2011.12.008.

He L, Chen JM, Liu J, Mo G, Bélair S, Zheng T, … Barr AG, 2014 Optimization of water uptake and photosynthetic parameters in an ecosystem model using tower flux data. Ecol. Model 294 (0), 94–104. 10.1016/j.ecolmodel.2014.09.019.

He LM, Liu J, Chen JM, Croft H, Wang R, Sprintsin M, … Zhang YQ, 2016 Inter- and intra-annual variations of clumping index derived from the MODIS BRDF product. Int. J. Appl. Earth Obs. Geoinf 44, 53–60.

He LM, Chen JM, Croft H, Gonsamo A, Luo XZ, Liu JN, … Liu Y, 2017a Nitrogen availability dampens the positive impacts of CO2 fertilization on terrestrial ecosystem carbon and water cycles. Geophys. Res. Lett 44 (22), 11590–11600. 10.1002/2017gl075981.

He L, Chen JM, Liu J, Bélair S, Luo X, 2017b Assessment of SMAP soil moisture for global simulation of gross primary production. Journal of Geophysical Research: Biogeosciences 122 10.1002/2016JG003603.

He L, Chen JM, Liu J, Mo G, Joiner J, 2017c Angular normalization of GOME-2 sun-induced chlorophyll fluorescence observation as a better proxy of vegetation productivity. Geophys. Res. Lett 10.1002/2017GL073708.

He L, Chen JM, Gonsamo A, Luo XZ, Wang R, Liu Y, Liu RG, 2018 Changes in the shadow: the shifting role of shaded leaves in global carbon and water cycles under climate change. Geophys. Res. Lett 45 (10), 5052–5061.

Hu S, Mo X, Lin Z, 2014 Optimizing the photosynthetic parameter Vcmax by assimilating MODIS-fPAR and MODIS-NDVI with a process-based ecosystem model. Agric. For. Meteorol 198–199, 320–334. 10.1016/j.agrformet.2014.09.002.

Iglesias MA, Law KJH, Stuart AM, 2013 Ensemble Kalman methods for inverse problems. Inverse Problems 29 (4), 045001. 10.1088/0266-5611/29/4/045001.

Ikawa H, Chen CP, Sikma M, Yoshimoto M, Sakai H, Tokida T, … Hasegawa T, 2018 Increasing canopy photosynthesis in rice can be achieved without a large increase in water use—a model based on free-air CO2 enrichment. Glob. Chang. Biol 24 (3), 1321–1341. 10.1111/gcb.13981. [PubMed: 29136323]

Jiao W, Chang Q, Wang L, 2019 The sensitivity of satellite solar-induced chlorophyll fluorescence to meteorological drought. Earth's Future 7 (5), 558–573. 10.1029/2018ef001087.

Jin P, Wang Q, Iio A, Tenhunen J, 2012 Retrieval of seasonal variation in photosynthetic capacity from multi-source vegetation indices. Ecological Informatics 7 (1), 7–18. 10.1016/j.ecoinf.2011.10.004.

Joiner J, Guanter L, Lindstrot R, Voigt M, Vasilkov AP, Middleton EM, … Frankenberg C, 2013 Global monitoring of terrestrial chlorophyll fluorescence from moderate-spectral-resolution near-infrared satellite measurements: methodology, simulations, and application to GOME-2. Atmos. Meas. Tech 6 (10), 2803–2823. 10.5194/amt-6-2803-2013.

Joiner J, Yoshida Y, Vasilkov A, Schaefer K, Jung M, Guanter L, … Marchesini LB, 2014 The seasonal cycle of satellite chlorophyll fluorescence observations and its relationship to vegetation phenology and ecosystem atmosphere carbon exchange. Remote Sens. Environ 152, 375–391.

Joiner J, Yoshida Y, Guanter L, Middleton EM, 2016 New methods for the retrieval of chlorophyll red fluorescence from hyperspectral satellite instruments: simulations and application to GOME-2 and SCIAMACHY. Atmos. Meas. Tech 9 (8), 3939–3967. 10.5194/amt-9-3939-2016.

Joiner J, Yoshida Y, Zhang Y, Duveiller G, Jung M, Lyapustin A, … Tucker C, 2018 Estimation of terrestrial global gross primary production (GPP) with satellite data-driven models and eddy covariance flux data. Remote Sens. 10 (9), 1346.

Kang BS, Singh K, Singh D, Garg BR, Lal R, Velayutham M, 2009 Viable alternatives to the rice-wheat cropping system in Punjab. J. Crop Improv 23 (3), 300–318. 10.1080/15427520902809912.

Kattge J, Knorr W, Raddatz T, Wirth C, 2009 Quantifying photosynthetic capacity and its relationship to leaf nitrogen content for global-scale terrestrial biosphere models. Glob. Chang. Biol 15 (4), 976–991.

Kattge J, Diaz S, Lavorel S, Prentice C, Leadley P, Bonisch G, … Wirth C, 2011 TRY - a global database of plant traits. Glob. Chang. Biol 17 (9), 2905–2935.

Kauwe MGD, Lin YS, Wright IJ, Medlyn BE, Crous KY, Ellsworth DS, … Domingues TF, 2016 A test of the 'one-point method' for estimating maximum carboxylation capacity from field-measured, light-saturated photosynthesis. New Phytol. 210 (3), 1130–1144. 10.1111/nph.13815. [PubMed: 26719951]

Khajuria A, 2016 Impact of nitrate consumption: case study of Punjab, India. Journal of Water Resource and Protection 8, 211–216. 10.4236/jwarp.2016.82017.

Koffi EN, Rayner PJ, Norton AJ, Frankenberg C, Scholze M, 2015 Investigating the usefulness of satellite-derived fluorescence data in inferring gross primary productivity within the carbon cycle data assimilation system. Biogeosciences 12 (13), 4067–4084. 10.5194/bg-12-4067-2015.

Köhler P, Frankenberg C, Magney TS, Guanter L, Joiner J, Landgraf J, 2018 Global retrievals of solar-induced chlorophyll fluorescence with TROPOMI: first results and intersensor comparison to OCO-2. Geophys. Res. Lett 45 (19), 10,456–410,463. 10.1029/2018gl079031.

Kunstler G, Falster D, Coomes DA, Hui F, Kooyman RM, Laughlin DC, … Westoby M, 2016 Plant functional traits have globally consistent effects on competition. Nature 529 (7585), 204–U174. [PubMed: 26700807]

Levine JM, 2016 A trail map for trait-based studies. Nature 529 (7585), 163–164. [PubMed: 26700809]

Li X, Xiao JF, He BB, 2018a Chlorophyll fluorescence observed by OCO-2 is strongly related to gross primary productivity estimated from flux towers in temperate forests. Remote Sens. Environ 204, 659–671.

Li X, Xiao J, He B, Altaf Arain M, Beringer J, Desai AR, … Varlagin A, 2018b Solar-induced chlorophyll fluorescence is strongly correlated with terrestrial photosynthesis for a wide variety of biomes: first global analysis based on OCO-2 and flux tower observations. Glob. Chang. Biol 24 (9), 3990–4008. 10.1111/gcb.14297. [PubMed: 29733483]

Liu Y, Liu RG, Chen JM, 2012 Retrospective retrieval of long-term consistent global leaf area index (1981–2011) from combined AVHRR and MODIS data. Journal of Geophysical Research-Biogeosciences 117.

Liu LY, Liu XJ, Wang ZH, Zhang B, 2016 Measurement and analysis of bidirectional SIF emissions in wheat canopies. IEEE Trans. Geosci. Remote Sens 54 (5), 2640–2651.

Liu L, Guan L, Liu X, 2017 Directly estimating diurnal changes in GPP for C3 and C4 crops using far-red sun-induced chlorophyll fluorescence. Agric. For. Meteorol 232, 1–9. 10.1016/j.agrformet.2016.06.014.

Luo X, Croft H, Chen JM, He L, Keenan TF, 2019 Improved estimates of global terrestrial photosynthesis using information on leaf chlorophyll content. Glob. Chang. Biol 0 (0). 10.1111/gcb.14624.

Luus KA, Commane R, Parazoo NC, Benmergui J, Euskirchen ES, Frankenberg C, … Lin JC, 2017 Tundra photosynthesis captured by satellite-observed solar-induced chlorophyll fluorescence. Geophys. Res. Lett 44 (3), 1564–1573. 10.1002/2016GL070842.

MacBean N, Maignan F, Bacour C, Lewis P, Peylin P, Guanter L, … Disney M, 2018 Strong constraint on modelled global carbon uptake using solar-induced chlorophyll fluorescence data. Sci. Rep 8 (1), 1973 10.1038/s41598-018-20024-w. [PubMed: 29386626]

Madani N, Kimball JS, Ballantyne AP, Affleck DLR, van Bodegom PM, Reich PB, … Running SW 2018 Future global productivity will be affected by plant trait response to climate. Sci. Rep 8.

Manter DK, Kerrigan J, 2004 A/Ci curve analysis across a range of woody plant species: influence of regression analysis parameters and mesophyll conductance. J. Exp. Bot 55 (408), 2581–2588. 10.1093/jxb/erh260. [PubMed: 15501912]

Massad RS, Tuzet A, Bethenod O, 2007 The effect of temperature on C4-type leaf photosynthesis parameters. Plant Cell Environ. 30 (9), 1191–1204. 10.1111/j.1365-3040.2007.01691.x. [PubMed: 17661755]

McKay MB, Alonso-Fradejas A, Brent ZW, Sauer S, Xu Y, 2016 China and Latin America: towards a new consensus of resource control? Third World Thematics: A TWQ Journal 1 (5), 592–611. 10.1080/23802014.2016.1344564.

Mier y Giménez Terán Cacho M, 2016 Soybean agri-food systems dynamics and the diversity of farming styles on the agricultural frontier in Mato Grosso, Brazil. J. Peasant Stud 43 (2), 419–441. 10.1080/03066150.2015.1016917.

Misson L, Tu KP, Boniello RA, Goldstein AH, 2006 Seasonality of photosynthetic parameters in a multi-specific and vertically complex forest ecosystem in the Sierra Nevada of California. Tree Physiol. 26 (6), 729–741. [PubMed: 16510388]

Mo X, Chen JM, Ju W, Black TA, 2008 Optimization of ecosystem model parameters through assimilating eddy covariance flux data with an ensemble Kalman filter. Ecol. Model 217 (1), 157–173. 10.1016/j.ecolmodel.2008.06.021.

Morgan PB, Bernacchi CJ, Ort DR, Long SP, 2004 An in vivo analysis of the effect of season-long open-air elevation of ozone to anticipated 2050 levels on photosynthesis in soybean. Plant Physiol. 135 (4), 2348–2357. 10.1104/pp.104.043968. [PubMed: 15299126]

Murchie EH, Lawson T, 2013 Chlorophyll fluorescence analysis: a guide to good practice and understanding some new applications. J. Exp. Bot 64 (13), 3983–3998. 10.1093/jxb/ert208. [PubMed: 23913954]

Norman JM, 1982 Simulation of microclimates In: Jerry H. (Ed.), Biometeorology in Integrated Pest Management. Academic Press, pp. 65–99.

Norton AJ, Rayner PJ, Koffi EN, Scholze M, Silver JD, Wang YP, 2018 Estimating global gross primary productivity using chlorophyll fluorescence and a data assimilation system with the BETHY-SCOPE model. Biogeosci. Discuss. 2018, 1–40. 10.5194/bg-2018-270.

Pinto F, Damm A, Schickling A, Panigada C, Cogliati S, Muller-Linow M, … Rascher U, 2016 Sun-induced chlorophyll fluorescence from high-resolution imaging spectroscopy data to quantify spatio-temporal patterns of photosynthetic function in crop canopies. Plant Cell and Environment 39 (7), 1500–1512.

Rezende LFC, Arenque BC, Aidar ST, Moura MSB, Von Randow C, Tourigny E, … Ometto JPHB (2016). Is the maximum velocity of carboxylation (Vcmax) well adjusted for deciduous shrubs in DGVMs? A case study for the Caatinga biome in Brazil. Modeling Earth Systems and Environment, 2(1), 42. doi:10.1007/s40808-016-0099-5.

Richards DG, 2010 Contradictions of the ‘new green revolution’: a view from South America’s southern cone. Globalizations 7 (4), 563–576. 10.1080/14747731.2010.505025.

Rienecker MM, Suarez MJ, Gelaro R, Todling R, Bacmeister J, Liu E, … Woollen J, 2011 MERRA: NASA’s modern-era retrospective analysis for research and applications. J. Clim 24 (14), 3624–3648.

Rogers A, Serbin SP, Ely KS, Sloan VL, Wullschleger SD, 2017 Terrestrial biosphere models underestimate photosynthetic capacity and CO2 assimilation in the Arctic. New Phytol. 216 (4), 1090–1103. 10.1111/nph.14740. [PubMed: 28877330]

Schöniger A, Nowak W, Hendricks Franssen H-J, 2012 Parameter estimation by ensemble Kalman filters with transformed data: approach and application to hydraulic tomography. Water Resour. Res 48 (4). 10.1029/2011wr010462.

Sharwood RE, Sonawane BV, Ghannoum O, 2014 Photosynthetic flexibility in maize exposed to salinity and shade. J. Exp. Bot 65 (13), 3715–3724. 10.1093/jxb/eru130. [PubMed: 24692650]

Silva-Pérez V, Furbank RT, Condon AG, Evans JR, 2017 Biochemical model of C3 photosynthesis applied to wheat at different temperatures. Plant Cell Environ. 40 (8), 1552–1564. 10.1111/pce.12953. [PubMed: 28338213]

Singh Y, Humphreys E, Kukal SS, Singh B, Kaur A, Thaman S, … Gajri PR, 2009 Crop performance in permanent raised bed rice-wheat cropping system in Punjab, India. Field Crop Res. 110 (1), 1–20.

Smith NG, Keenan TF, Colin Prentice I, Wang H, Wright IJ, Niinemets Ü, … Zhou S-X, 2019 Global photosynthetic capacity is optimized to the environment. Ecol. Lett 22 (3), 506–517. 10.1111/ele.13210. [PubMed: 30609108]

Sun Y, Fu R, Dickinson R, Joiner J, Frankenberg C, Gu L, … Fernando N, 2015a Drought onset mechanisms revealed by satellite solar-induced chlorophyll fluorescence: insights from two contrasting extreme events. Journal of Geophysical Research: Biogeosciences 120 (11), 2427–2440. 10.1002/2015jg003150.

Sun JS, Sun JD, Feng ZZ, 2015b Modelling photosynthesis in flag leaves of winter wheat (Triticum aestivum) considering the variation in photosynthesis parameters during development. Funct. Plant Biol 42 (11), 1036–1044. [PubMed: 32480743]

Sun Y, Frankenberg C, Wood JD, Schimel DS, Jung M, Guanter L, … Yuen K, 2017a OCO-2 advances photosynthesis observation from space via solar-induced chlorophyll fluorescence. Science 358 (6360). 10.1126/science.aam5747.

Sun Y, Frankenberg C, Wood JD, Schimel DS, Jung M, Guanter L, … Yuen K, 2017b OCO-2 advances photosynthesis observation from space via solar-induced chlorophyll fluorescence. Science 358 (6360), eaam5747. 10.1126/science.aam5747.

Sun Y, Frankenberg C, Jung M, Joiner J, Guanter L, Köhler P, Magney T, 2018 Overview of solar-induced chlorophyll fluorescence (SIF) from the Orbiting Carbon Observatory-2: retrieval, cross-mission comparison, and global monitoring for GPP. Remote Sens. Environ 209, 808–823. 10.1016/j.rse.2018.02.016.

Torres SM, Moran EF, Silva RFB, 2017 Property rights and the soybean revolution: shaping how China and Brazil are telecoupled. Sustainability 9 (6).

van der Tol C, Verhoef W, Timmermans J, Verhoef A, Su Z, 2009. An integrated model of soil-canopy spectral radiances, photosynthesis, fluorescence, temperature and energy balance. Biogeosciences 6 (12), 3109–3129. 10.5194/bg6-3109-2009.

Verhoef W, 1984 Light scattering by leaf layers with application to canopy reflectance modeling: the SAIL model. Remote Sens. Environ 16 (2), 125–141. 10.1016/0034-4257(84)90057-9.

Verma M, Schimel D, Evans B, Frankenberg C, Beringer J, Drewry DT, … Eldering A, 2017 Effect of environmental conditions on the relationship between solar-induced fluorescence and gross primary productivity at an OzFlux grassland site. Journal of Geophysical Research: Biogeosciences. 10.1002/2016JG003580. n/a-n/a.

Verrelst J, van der Tol C, Magnani F, Sabater N, Rivera JP, Mohammed G, Moreno J, 2016 Evaluating the predictive power of sun-induced chlorophyll fluorescence to estimate net photosynthesis of vegetation canopies: a SCOPE modeling study. Remote Sens. Environ 176, 139–151.

Wagle P, Zhang Y, Jin C, Xiao X, 2016 Comparison of solar-induced chlorophyll fluorescence, light-use efficiency, and process-based GPP models in maize. Ecol. Appl 26 (4), 1211–1222. 10.1890/15-1434. [PubMed: 27509759]

Walker AP, Beckerman AP, Gu L, Kattge J, Cernusak LA, Domingues TF, … Woodward FI, 2014 The relationship of leaf photosynthetic traits – Vcmax and Jmax – to leaf nitrogen, leaf phosphorus, and specific leaf area: a meta-analysis and modeling study. Ecology and Evolution 4 (16), 3218–3235. 10.1002/ece3.1173. [PubMed: 25473475]

Walker BJ, Drewry DT, Slattery RA, VanLoocke A, Cho YB, Ort DR, 2017a Chlorophyll can be reduced in crop canopies with little penalty to photosynthesis. Plant Physiol. 10.1104/pp.17.01401.

Walker AP, Quaife T, Bodegom PM, Kauwe MGD, Keenan TF, Joiner J, … Woodward FI (2017b). The impact of alternative trait-scaling hypotheses for the maximum photosynthetic carboxylation rate (Vcmax) on global gross primary production. New Phytol., 215(4), 1370–1386. doi:10.1111/nph.14623. [PubMed: 28643848]

Walther S, Voigt M, Thum T, Gonsamo A, Zhang YG, Kohler P, … Guanter L, 2016 Satellite chlorophyll fluorescence measurements reveal large-scale decoupling of photosynthesis and greenness dynamics in boreal evergreen forests. Glob. Chang. Biol 22 (9), 2979–2996. 10.1111/gcb.13200. [PubMed: 26683113]

Wang Q, 2008 Annual and seasonal variations in photosynthetic capacity of Fagus crenata along an elevation gradient in the Naeba Mountains, Japan. Tree Physiol 28 (2), 277–285. -2008 v.2028 no.2002. 10.1093/treephys/28.2.277.

Wang Z, 2014 Sunlit Leaf Photosynthesis Rate Correlates Best With Chlorophyll Fluorescence of Terrestrial Ecosystems (Master of Science). University of Toronto, Toronto.

Wang Q, Tenhunen J, Falge E, Bernhofer C, Granier A, Vesala T, 2004 Simulation and scaling of temporal variation in gross primary production for coniferous and deciduous temperate forests. Glob. Chang. Biol 10 (1), 37–51. 10.1111/j.1365-2486.2003.00716.x.

Wang Q, Tenhunen J, Vesala T, 2009a Correlated change in normalized difference vegetation index and the seasonal trajectory of photosynthetic capacity in a conifer stand. Int. J. Remote Sens 30 (4), 983–1001. 10.1080/01431160802427905.

Wang Q, Tenhunen J, Vesala T, 2009b Gross primary production simulation in a coniferous forest using a daily gas exchange model with seasonal change of leaf physiological parameters derived from remote sensing data. Int. J. Remote Sens 30 (12), 3013–3025. 10.1080/01431160802558691.

Wang R, Chen JM, Pavlic G, Arain A, 2016 Improving winter leaf area index estimation in coniferous forests and its significance in estimating the land surface albedo. ISPRS J. Photogramm. Remote Sens 119, 32–48. 10.1016/j.isprsjprs.2016.05.003.

Wood JD, Griffis TJ, Baker JM, Frankenberg C, Verma M, Yuen K, 2017 Multiscale analyses of solar-induced florescence and gross primary production. Geophys. Res. Lett 44 (1), 533–541. 10.1002/2016GL070775.

Xiao J, Li X, He B, Arain MA, Beringer J, Desai AR, … Varlagin A, 2019 Solar-induced chlorophyll fluorescence exhibits a universal relationship with gross primary productivity across a wide variety of biomes. Glob. Chang. Biol 25 (4), e4–e6. 10.1111/gcb.14565.

Xu LK, Baldocchi DD, 2003 Seasonal trends in photosynthetic parameters and stomatal conductance of blue oak (Quercus douglasii) under prolonged summer drought and high temperature. Tree Physiol. 23 (13), 865–877. [PubMed: 14532010]

Xu GL, Singh SK, Reddy VR, Barnaby JY, Sicher RC, Li T, 2016 Soybean grown under elevated CO2 benefits more under low temperature than high temperature stress: varying response of photosynthetic limitations, leaf metabolites, growth, and seed yield. J. Plant Physiol 205, 20–32. [PubMed: 27589223]

Yang X, Tang JW, Mustard JF, Lee JE, Rossini M, Joiner J, … Richardson AD, 2015 Solar-induced chlorophyll fluorescence that correlates with canopy photosynthesis on diurnal and seasonal scales in a temperate deciduous forest. Geophys. Res. Lett 42 (8), 2977–2987.

Yang H, Yang X, Zhang Y, Heskel MA, Lu X, Munger JW, … Tang J, 2016 Chlorophyll fluorescence tracks seasonal variations of photosynthesis from leaf to canopy in a temperate forest. Glob. Chang. Biol 10.1111/gcb.13590. n/a-n/a.

Yang X, Shi H, Stovall A, Guan K, Miao G, Zhang Y, … Lee J-E, 2018 FluoSpec 2—an automated field spectroscopy system to monitor canopy solar-induced fluorescence. Sensors 18 (7), 2063.

Yoshida Y, Joiner J, Tucker C, Berry J, Lee JE, Walker G, … Wang Y, 2015 The 2010 Russian drought impact on satellite measurements of solar-induced chlorophyll fluorescence: insights from modeling and comparisons with parameters derived from satellite reflectances. Remote Sens. Environ 166, 163–177.

Zhang YG, Guanter L, Berry JA, Joiner J, van der Tol C, Huete A, … Kohler P, 2014 Estimation of vegetation photosynthetic capacity from space-based measurements of chlorophyll fluorescence for terrestrial biosphere models. Glob. Chang. Biol 20 (12), 3727–3742. 10.1111/gcb.12664. [PubMed: 24953485]

Zhang Y, Guanter L, Berry JA, van der Tol C, Yang X, Tang J, Zhang F, 2016a Model-based analysis of the relationship between sun-induced chlorophyll fluorescence and gross primary production for remote sensing applications. Remote Sens. Environ 187, 145–155. 10.1016/j.rse.2016.10.016.

Zhang Y, Xiao X, Jin C, Dong J, Zhou S, Wagle P, … Moore Iii B, 2016b Consistency between sun-induced chlorophyll fluorescence and gross primary production of vegetation in North America. Remote Sens. Environ 183, 154–169. 10.1016/j.rse.2016.05.015.

Zhang Y, Guanter L, Joiner J, Song L, Guan K, 2018a Spatially-explicit monitoring of crop photosynthetic capacity through the use of space-based chlorophyll fluorescence data. Remote Sens. Environ 210, 362–374. 10.1016/j.rse.2018.03.031.

Zhang Z, Zhang Y, Joiner J, Migliavacca M, 2018b Angle matters: bidirectional effects impact the slope of relationship between gross primary productivity and sun-induced chlorophyll fluorescence from Orbiting Carbon Observatory-2 across biomes. Glob. Chang. Biol 24 (11), 5017–5020. 10.1111/gcb.14427. [PubMed: 30136335]

Zheng T, Chen J, He L, Arain MA, Thomas SC, Murphy JG, … Black TA, 2017 Inverting the maximum carboxylation rate (Vcmax) from the sunlit leaf photosynthesis rate derived from measured light response curves at tower flux sites. Agric. For. Meteorol 236, 48–66. 10.1016/j.agrformet.2017.01.008.

Zhu X, Chen J, Qiu K, Kuai B, 2017 Phytohormone and light regulation of chlorophyll degradation. Front. Plant Sci 8 (1911). 10.3389/fpls.2017.01911.

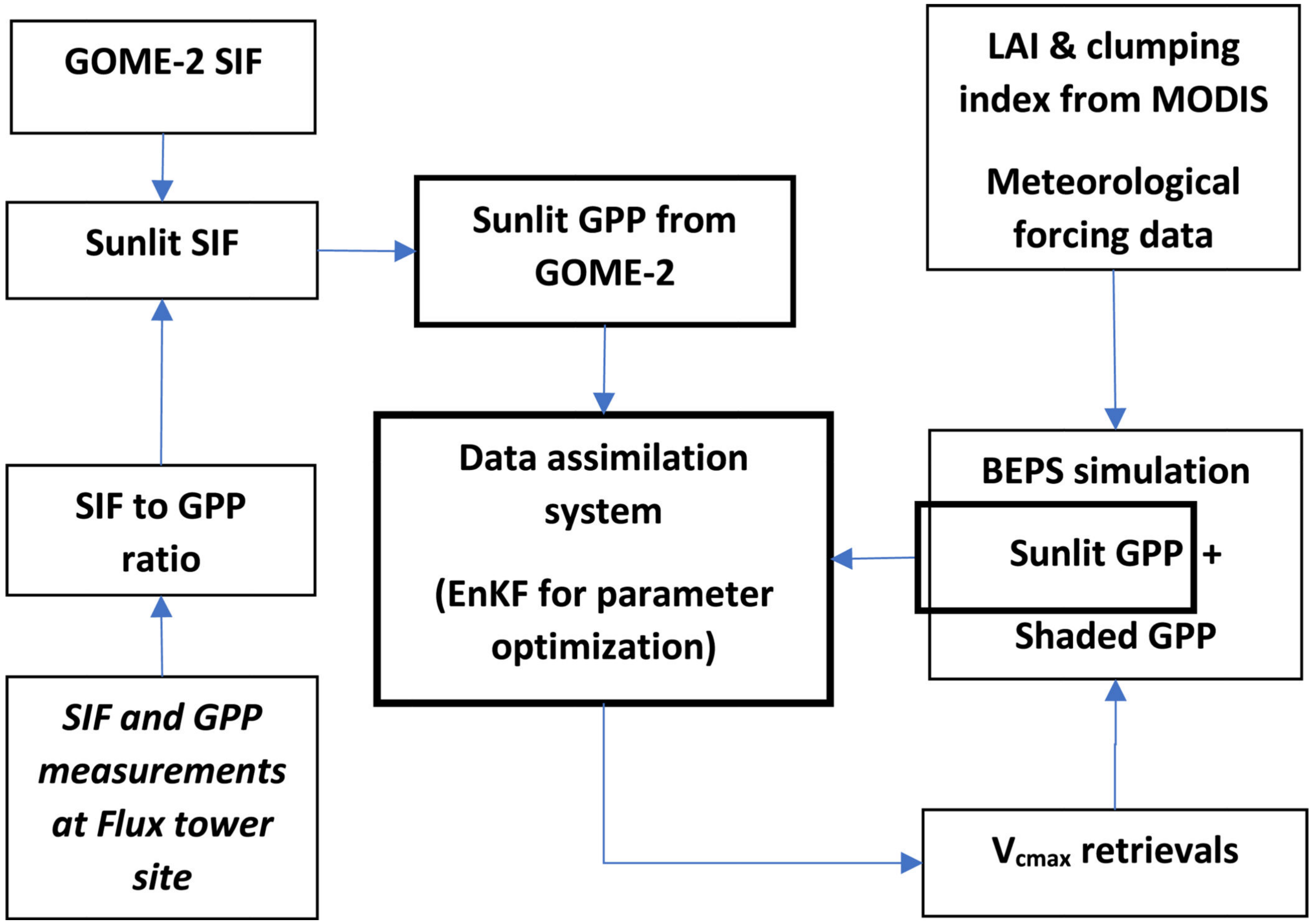

Fig. 1.

The parameter optimization framework for retrieving top-of-canopy V_{cmax} from sun-induced chlorophyll fluorescence (SIF) measurements in a data assimilation system (bold frames).

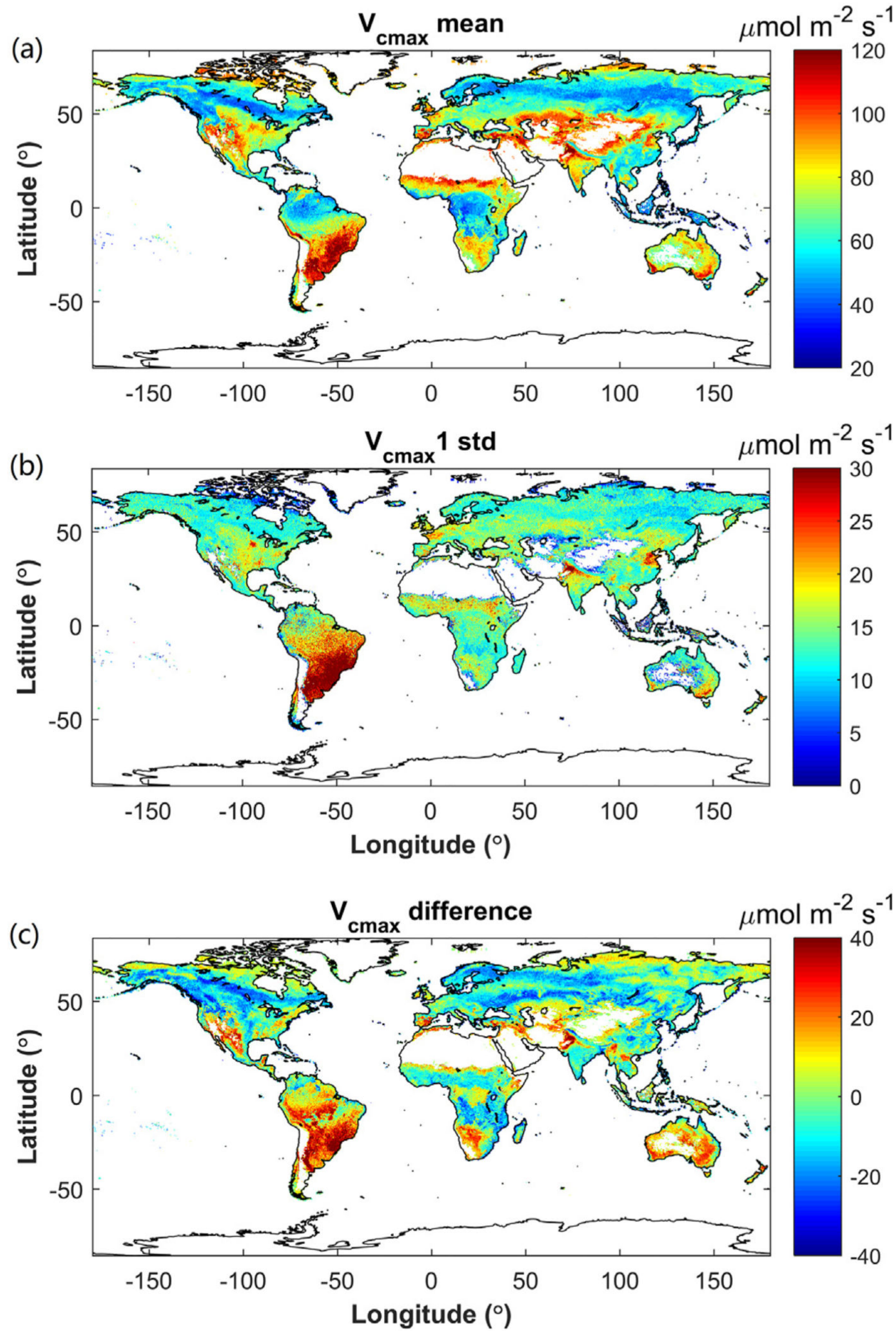

Fig. 2.

Global top-of-canopy V_{cmax} normalized to 25 °C derived from 11-year (2007–2017) SIF data. (a) Multi-year average of V_{cmax} map weighted by GPP. (b) The seasonal and inter-annual variation of V_{cmax} represented by one standard deviation. (c) The difference between SIF-derived V_{cmax} and BEPS-default V_{cmax}.

NASA Author Manuscript
NASA Author Manuscript

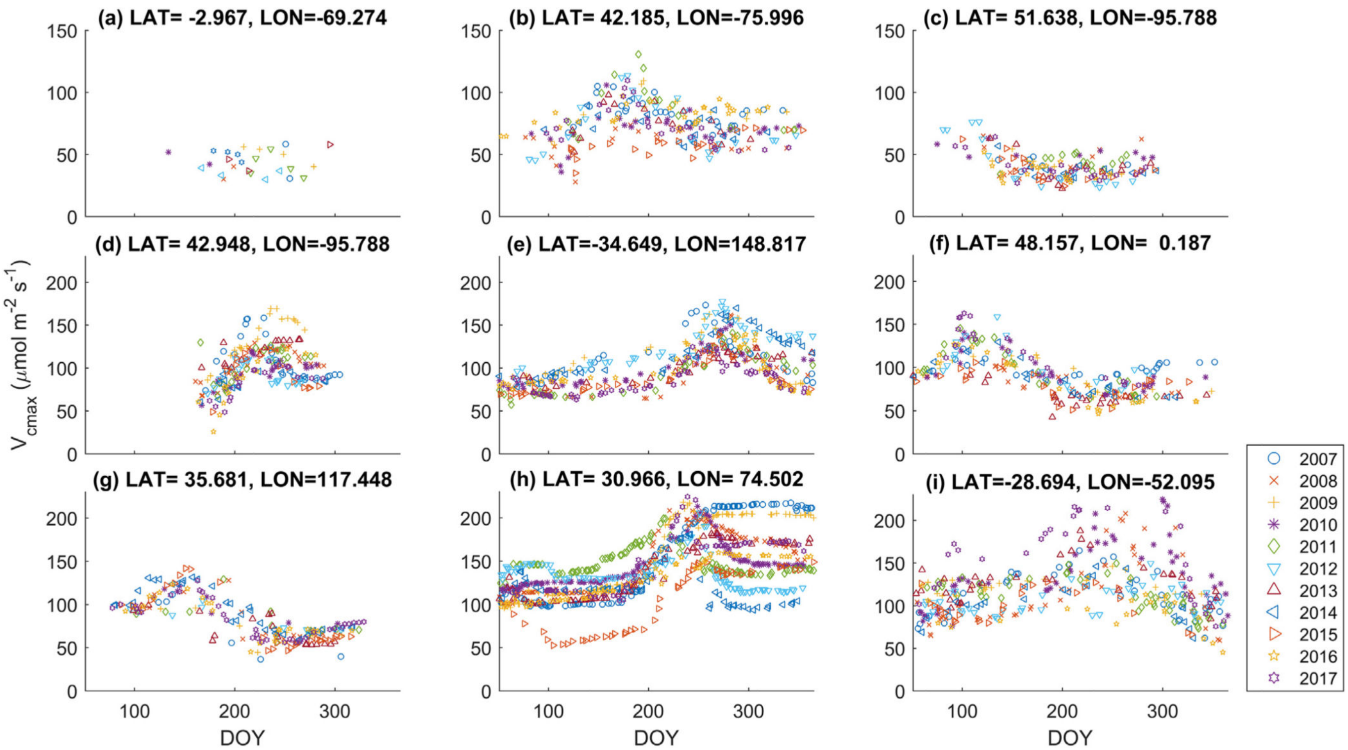

Fig. 3.

Top-of-canopy V_{cmax} normalized to 25 °C for different plant function types at 36 km resolution. (a) EBF at Amazon. (b) DBF at US. (c) ENF at boreal forest, Canada. (d) Cropland in US corn belt. (e) Cropland in Australia. (f) Cropland in France. (g) Cropland (wheat-corn system) in China. (h) Cropland (wheat-rice system) in Punjab, India. (i) Crop/forest mixed pixel in South America. LAT indicates latitude, and LON indicates longitude.

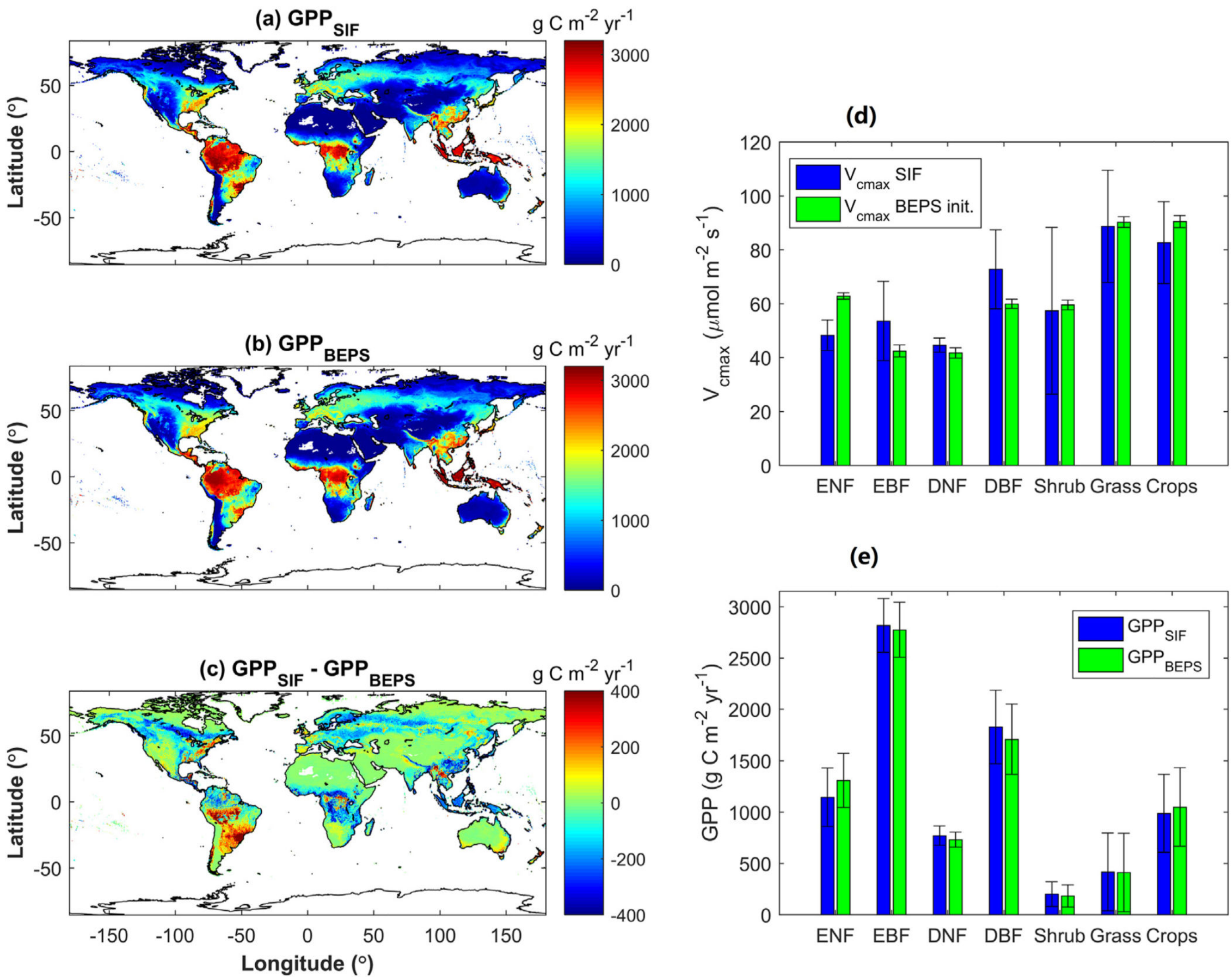

Fig. 4.

Impacts of the SIF-derived global V_{cmax} map. (a) Annual GPP in 2007–2016 constrained by SIF. (b) Annual GPP in 2007–2016 using default V_{cmax} values. (c) The GPP difference between (a) and (b). (d) Comparison of SIF-derived V_{cmax} and BEPS-default V_{cmax} for each plant function type. (e) Comparison of GPP simulations w/o SIF-constraint. The values in (d) and (e) are listed in Supplementary tables.

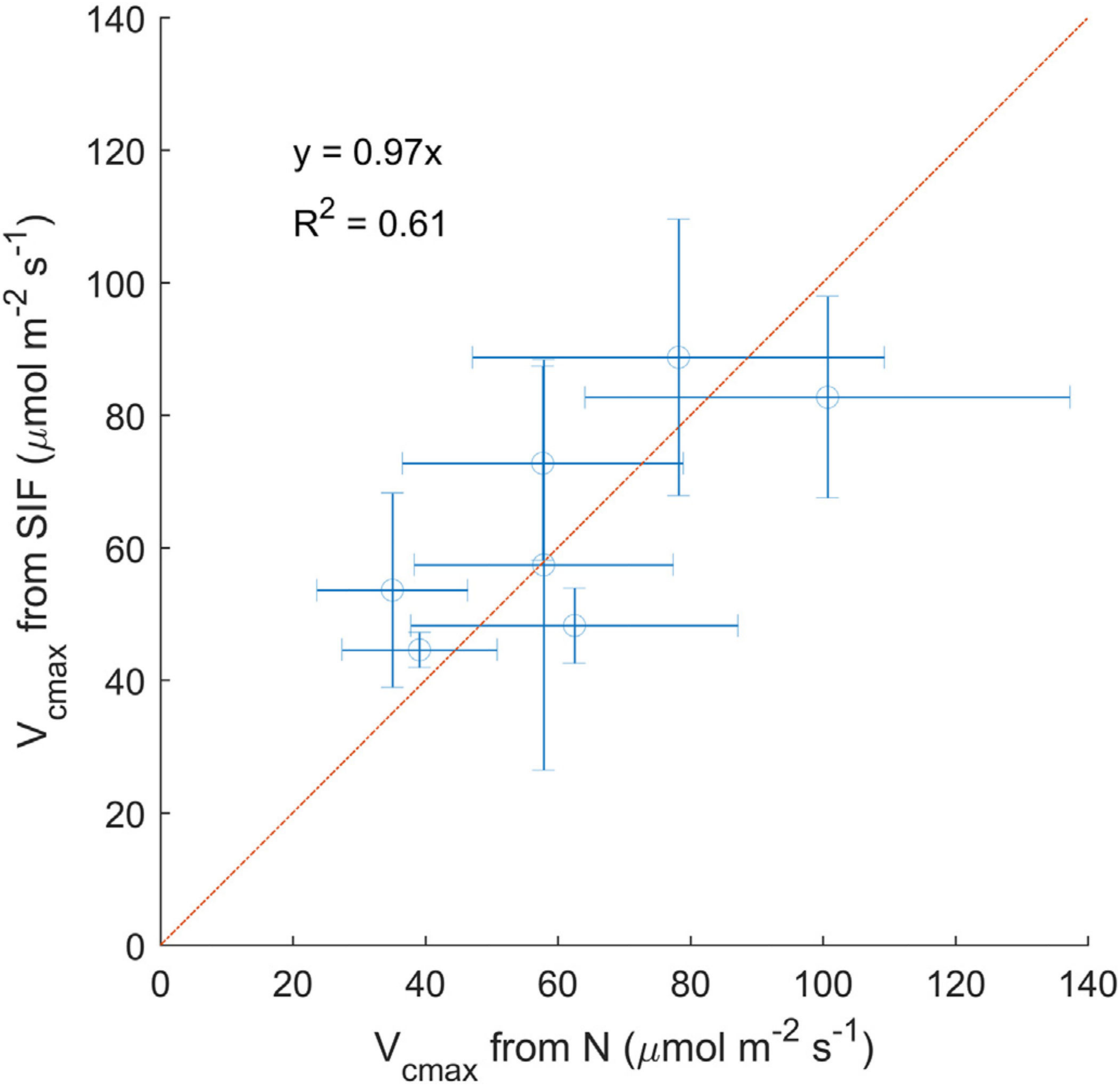

Fig. 5.

Comparison of SIF-derived V_{cmax} from this study to N-derived* V_{cmax} (Kattge et al., 2009) for seven plant function types.

NASA Author Manuscript

NASA Author Manuscript

Table 1

Top-of-canopy V_{cmax} (μmol m^{-2} s^{-1}) normalized to 25 °C for different plant function types (Evergreen Needle-leaf trees, ENF; Evergreen Broadleaf trees, EBF; Deciduous Needle-leaf trees, DNF; Deciduous Broadleaf trees, DBF). "SIF" indicates V_{cmax} derived from SIF measurements; "BEPS" indicates the initial V_{cmax} values in BEPS.

	Count	V_{cmax} (SIF)	V_{cmax} 1 std. (SIF)	V_{cmax} (BEPS)	V_{cmax} 1 std. (BEPS)
ENF	1954	48.2	5.7	62.8	1.2
EBF	8230	53.6	14.7	42.4	2.2
DNF	667	44.6	2.7	41.7	1.9
DBF	1071	72.7	14.7	59.9	1.7
Shrub	10,420	57.4	31.0	59.5	1.8
Grass	8022	88.7	20.9	90.3	2.0
Crops	2432	82.7	15.2	90.5	2.2

Table 2

GPP values (g C m^{-2} s^{-1}) simulated using SIF-retrieved V_{cmax} and default V_{cmax} in BEPS for different each plant function types.

	Count	GPP (SIF)	GPP 1 std. (SIF)	GPP (BEPS)	GPP 1 std. (BEPS)
ENF	1954	1143.6	284.7	1307.6	263.3
EBF	8230	2817.6	261.8	2774.0	267.7
DNF	667	770.1	93.4	731.0	73.1
DBF	1071	1827.4	358.6	1708.5	342.4
Shrub	10,420	200.3	119.5	182.5	108.9
Grass	8022	415.7	378.9	411.0	382.9
Crops	2432	986.9	379.8	1049.1	380.9